Energy Storage Materials 29 (2020) 9–16

Contents lists available at ScienceDirect

Energy Storage Materials

journal homepage: www.elsevier.com/locate/ensm

Structural engineering of hydrated vanadium oxide cathode by K^+ incorporation for high-capacity and long-cycling aqueous zinc ion batteries

Meng Tian [a,b,1], Chaofeng Liu [a,1], Jiqi Zheng [a], Xiaoxiao Jia [a], Evan P. Jahrman [c], Gerald T. Seidler [c], Donghui Long [b,d,**], Muhammad Atif [e], Mohamad Alsalhi [e], Guozhong Cao [a,*]

[a] Department of Materials Science and Engineering, University of Washington, Seattle, WA, 98195, USA
[b] State Key Laboratory of Chemical Engineering, East China University of Science and Technology, Shanghai, 200237, China
[c] Department of Physics, University of Washington, Seattle, WA, 98195-1560, United States
[d] Shanghai Key Laboratory of Multiphase Materials Chemical Engineering, East China University of Science and Technology, Shanghai, 200237, China
[e] Physics and Astronomy Department, College of Science, King Saud University, Riyadh, 11451, Saudi Arabia

ARTICLE INFO

Keywords:
Zinc ion batteries
K^+ incorporation
Hydrated vanadate
High capacity
Structural engineering

ABSTRACT

Vanadium oxides are promising candidates for cathode materials in aqueous zinc-ion batteries (ZIBs) with low cost and high capacity yet requirements for long cycling necessitate the development of increasingly stable structure. This study reports a structural engineering method by incorporating K^+ into hydrated vanadium pentoxide ($V_2O_5{\cdot}nH_2O$, VOH) to achieve unique hydrated vanadate ($KV_{12}O_{30\text{-}y}{\cdot}nH_2O$, KVOH). In contrast to previously reported works, K^+ introduction leads to a new phase of KVOH with faster ion diffusion kinetics and better long-term cycling stability. This work establishes an understanding of the role of K^+ incorporation in KVOH which goes beyond its conventional categorization as an agent for interlayer spacing adjustment, reflecting in maintaining structure flexibility for effective Zn^{2+} insertion/extraction even at high rates, improving materials conductivity by the electron hoping of V^{4+}/V^{5+} and acting as a stabilizer to accommodate structural contraction/expansion with smaller voltage hysteresis and higher reversibility. KVOH displays a remarkable capacity of 436 mAh g^{-1} at 0.05 A g^{-1}, maintains 227 mAh g^{-1} at 10 A g^{-1}, which is better than VOH and the majority of reported monovalent and multivalent metal ions introduced in vanadates. KVOH exhibits excellent cycling stability with 92% capacity retention over 3000 cycles at 5 A g^{-1}, high energy density (308 Wh kg^{-1}) and power density (7502 W kg^{-1}), as well as improved energy efficiency. These characteristics recommend KVOH cathodes for use in high-performance aqueous ZIBs.

1. Introduction

Ever-increasing energy consumption and continuous environmental concerns drive higher requirements for next-generation energy storage and conversion systems [1–3]. Lithium-ion batteries (LIBs) and sodium-ion batteries (SIBs) have achieved commercial success with high energy densities but are restricted by high prices, limited resources and/or safety concerns [4,5]. Reversible aqueous batteries are emerging energy storage candidates and have attracted tremendous attentions in recent years, especially aqueous zinc ion batteries (ZIBs) [6–8]. Regarding anodes for ZIBs, Zn metal possesses high abundance in the Earth's crust (79 ppm), low redox potential (−0.76 V vs. standard hydrogen electrode), high theoretical capacity (820 mAh g^{-1}, 5851 mAh cm^{-3}) and great moisture tolerance [9,10]. Aqueous electrolytes are environmentally friendly, safe during operation and transportation, and highly ionic conductive (up to 1 S cm^{-1}), over two magnitudes greater than organic electrolytes (1–10 mS cm^{-1}) [11]. Cathode materials in ZIBs comprise the main research hotspot for achieving improved energy density and excellent cycling stability, including vanadium oxides [12,13], manganese oxides [14,15], Prussian Blue and its analogs [16,17]. Manganese oxides possess the capacity of about 300 mAh g^{-1} but an irreversible phase transition leads to capacity decay during long-term cycling [18]. Prussian Blue and its analogs exhibit tunable structure with mixed-valence hexacyanoferrate but are hindered by low capacities

* Corresponding author.
** Corresponding author. State Key Laboratory of Chemical Engineering, East China University of Science and Technology, Shanghai, 200237, China.
E-mail addresses: longdh@mail.ecust.edu.cn (D. Long), gzcao@uw.edu (G. Cao).
[1] M. Tian and C. Liu contributed equally.

https://doi.org/10.1016/j.ensm.2020.03.024
Received 25 February 2020; Received in revised form 23 March 2020; Accepted 26 March 2020
Available online 31 March 2020
2405-8297/Published by Elsevier B.V.

of below 100 mAh g^{-1} [19]. Vanadium oxides show a superior capacity of 400 mAh g^{-1} and simultaneously low cost less than \$11 lb^{-1}, with considerable practicality for portable electronics, electric vehicles and large-scale energy storage stations [20–22]. However, poor structural stability at high rates and during long cycling should be further improved to meet practical requirements [23].

Researchers mainly focus on introducing water molecules or metal cations into vanadium oxides to achieve larger interlayer spacing for fast ion transfer and better electrochemical stability [24,25]. The structural water molecules between adjacent layers in vanadium pentoxide (V_2O_5) effectively expand the interlayer spacing from 8.75 Å to 10.76 Å, providing more open channels for Zn^{2+} transfer [20]. And the shielding effect of water molecules can reduce the effective charge of Zn^{2+} and weaken electrostatic interaction between Zn^{2+} and the V_2O_5 framework to enhance Zn^{2+} intercalation kinetics [26,27]. Transition metal cations can further broaden the lattice spacing and more importantly promote structural stability. Manganese expanded hydrated vanadate (MnVO) with interlayer spacing of 12.9 Å demonstrates a high capacity of 415 mAh g^{-1} at a current density of 0.05 A g^{-1} and maintains 92% capacity retention after 2000 cycles, which is significantly superior to hydrated vanadium pentoxide (VOH) due to the "pillar" effect of Mn^{2+} on structure stability [28]. Ni^{2+}, Zn^{2+} and La^{3+} intercalated hydrated vanadates are also fabricated to achieve electrochemical performance improvement [28–30]. Moreover, researchers discovered low-cost alkaline metal cations play the same "pillar" role in stabilizing vanadate structure just like transition metal cations [31,32]. K^+ with larger ionic radius (0.138 nm) illustrates a better relief of electrostatic resistance for Zn^{2+} transfer than Li^+ (0.076 nm) and Na^+ (0.102 nm) [33]. Tang et al. [34] fabricated various potassium vanadates ($K_2V_8O_{21}$, $K_{0.25}V_2O_5$, $K_2V_6O_{16}{\cdot}1.57H_2O$ and KV_3O_8), $K_2V_8O_{21}$ with the large interlayer space of 14.8 Å shows the optimal electrochemical performance with 247 mAh g^{-1} at 0.3 A g^{-1} and good cycling stability at 6 A g^{-1} over 300 cycles. Sambandam et al. [35] prepared $K_2V_6O_{16}{\cdot}2.7H_2O$ with more crystalline water in the structure while it just shows the lattice spacing of 7.5 Å. But it delivers 330 mAh g^{-1} at 0.2 A g^{-1} after 53 cycles and retains 82% capacity retention after 500 charge/discharge cycles at 2 A g^{-1}. However, in reported hydrated potassium vanadates K^+ was just preinserted into V_2O_5 layers to achieve interlayer spacing adjustment but not introduced into V_2O_5 crystal lattice to form a new phase.

The present work investigates the fabrication and the detailed structural and electrochemical characterization of K^+ stabilized hydrated vanadate (KVOH). It is a new phase compared to hydrated vanadium pentoxide ($V_2O_5{\cdot}nH_2O$, VOH), with the contracted interlayer spacing of 9.9 Å than VOH of 12.0 Å, but still demonstrates fast ion diffusion and enhanced reaction kinetics with a capacity up to 436 mAh g^{-1} at 0.05 A g^{-1}, high energy efficiency with excellent charge/discharge reversibility, and great electrochemical stability with 92% capacity retention at 5 A g^{-1} after 3000 cycles. The impacts of the incorporation of K^+ in KVOH on crystal and microstructures, chemical and electrochemical properties, as well as zinc ion battery performance have been elaborated and discussed.

2. Results and discussion

KVOH was prepared by a facile one-step hydrothermal method without further annealing (the details are given in the Experimental Section in SI). The SEM image in Fig. 1a exhibits urchin-like microspheres of KVOH consisting of numerous nanorods with the diameter around 20 nm as verified by TEM in Fig. 1b. The corresponding elemental mappings with uniform distribution of elements K, V and O in KVOH nanorods are in agreement with the profile of the image. The typical lattice fringes can be observed in HR-TEM image in Fig. 1c, with the interlayer spacing of 1.9 Å relating to the diffraction peak at 47.5° in XRD patterns (Fig. 1d). Selected area electron diffraction (SAED) pattern inset in Fig. 1c is also in coincidence with the same diffraction peak with the

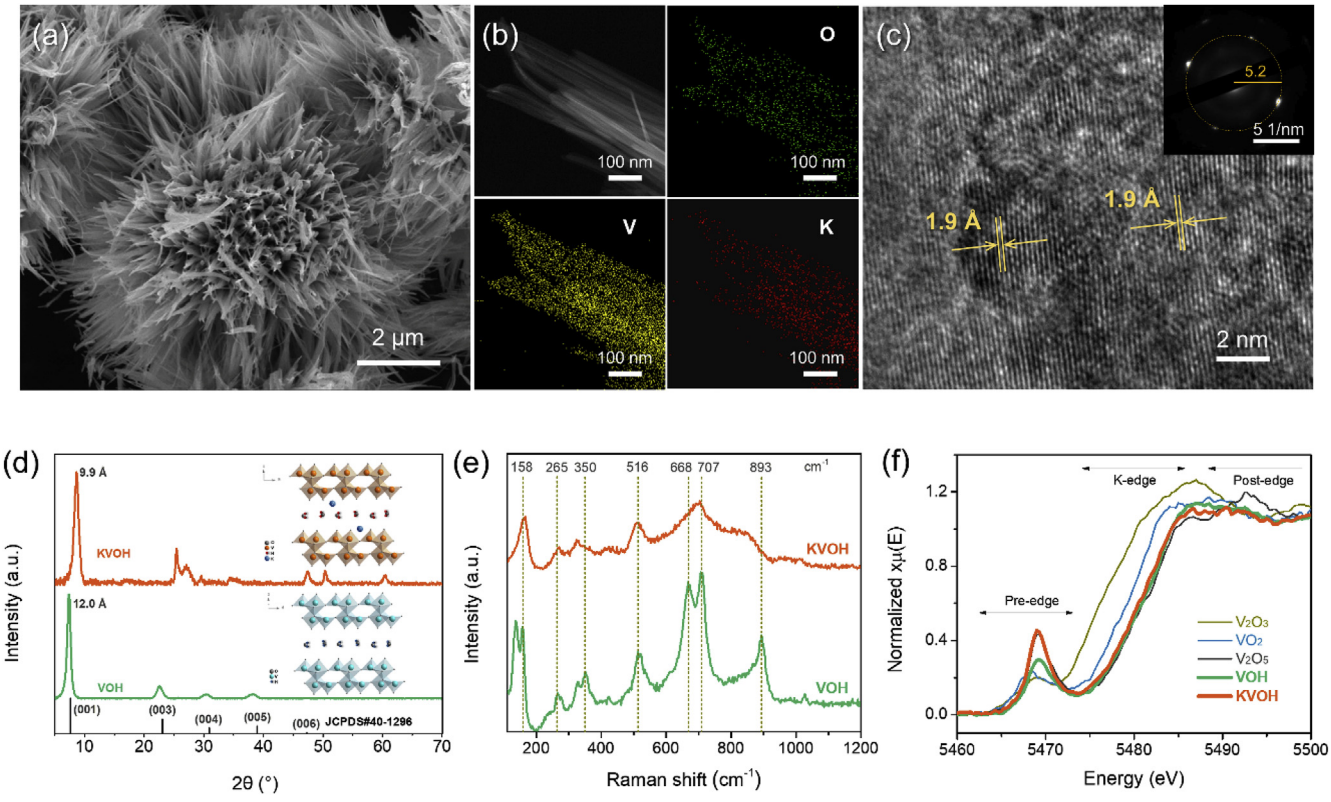

Fig. 1. (a) SEM image, (b) TEM image and elemental mappings and (c) HR-TEM image (inset is SAED pattern) of KVOH, showing an urchin-like structure with the homogeneous elemental distribution. (d) XRD patterns (inset are possible schematic frameworks) and (e) Raman spectra of samples. (f) V K-edge XANES spectra of samples and empirical standards.

same lattice spacing shown in HR-TEM. VOH was synthesized by the similar hydrothermal method but without adding K^+ precursor. The morphology of VOH is shown in Fig. S1a. The lattice fringes of VOH in Fig. S1b exhibit a lattice spacing of 1.9 Å, corresponding to (006) facet. Although the same lattice spacing was observed in KVOH, it does not indicate the same crystal facet information as the crystal structure of KVOH is different from that of VOH. XRD patterns in Fig. 1d provide more information about the crystalline structure of samples. VOH performs a typical bilayer structure similar to $V_2O_5{\cdot}1.6H_2O$ (JCPDS #40–1296), composed of [VO_5] and [VO_6] polyhedron and water molecules between layers (inset in Fig. 1d). Structural water plays an important role in screening charges as "lubricants" for effective Zn^{2+} diffusion [26]. For KVOH, it demonstrates a unique XRD pattern, different from that reported in the literature with K^+ incorporated into the structure [34,35]. The standard XRD pattern of KVOH could not be provided based on the latest database. Compared to VOH, KVOH exhibits a contracted lattice spacing of 9.9 Å, smaller than 12.0 Å of VOH, an indication of structure shrinkage after K^+ introduction. TG results in Fig. S2 indicate KVOH (8 wt%) with less interlayer water than VOH (12 wt%). This phenomenon is different from the enlarged interlayer spacing with the incorporation of transition metal cations (e.g. Mn, Ni and Co) [28]. The exact mechanism leading to the contraction of the interlayer spacing is not known and requires more fundamental study, however, it may be due to the strong interaction of K^+ with oxygen anions in bilayers results in K–O bond formation and the lattice spacing reduction [36]. The ionic character value of chemical bonds can be estimated based on the equation as follows [37,38].

$$\%\text{ionic character} = 100 - 100 \times exp\left[-0.25\,(X_a - X_b)^2\right] \quad (1)$$

where $X_a$and X_b are the electronegativity of anion and cation, respectively. Compared to M − O bond (M: Mn, Ni, Co), K–O bond shows a higher ionic character value of 82% due to lower electronegativity of K, with higher binding energy. Raman spectra in Fig. 1e show the stretching and bending vibrations of chemical bonds. For VOH, the peaks located at 158, 265, 350 cm^{-1} correspond to –O–V–O–V– chains, V═O and interlayer water, respectively [39]. The peak at 516 and 707 cm^{-1} suggests the V_3–O (triply coordinated oxygen) bond and the V_2–O (doubly coordinated oxygen) bond, respectively [40]. Differently, VOH shows a distinguished peak at 668 cm^{-1} attributed to disordered V_2–O in the structure [41] while KVOH has only a broadened peak at 707 cm^{-1}. It could be ascribed to K^+ introduction leads to an enhanced interaction and better crystallinity. The peak at 893 cm^{-1} for VOH relates to the V–OH_2 bond [42]. A redshift of this peak for KVOH illustrates the weakened V–OH_2 bond induced by K^+ introduction having interaction between K^+ and interlayer water. X-ray absorption near edge structure (XANES) measurements were used to reveal the oxidation state and local coordination environment of V in the bulk of KVOH and VOH [43,44]. Fig. 1f reveals that KVOH and VOH illustrate similar K-edge position to that of V_2O_5, which served as an empirical standard representing a predominantly V^{5+} material. A slight edge shift to lower photon energies indicates some lower-valence V in KVOH and VOH [45], which is confirmed by fitting results, with 27% and 14% of V^{4+} in KVOH and VOH, respectively, fitting details are shown in SI. The peak in the pre-edge region corresponds to transitions from 1s to nominally 3 d empty orbitals. The peak intensity varies with the coordination geometry, higher intensity means a lower central symmetry of coordination (e.g. tetrahedral > square-pyramidal > octahedral) as the absence of inversion symmetry permits hybridization of the empty 3d orbitals with orbitals of dipole-allowed p character [46,47]. KVOH and VOH show distinct pre-edge peak, which is attributed to 5-coordinated [VO_5] polyhedra. KVOH exhibits a higher peak intensity than VOH, an indication of a structure distortion after K^+ introduction. V $2p_{3/2}$ XPS spectra are shown in Fig. S3 to reveal the V valence on the sample's surface. It can be decomposed into two peaks at 517.4 eV and 516.4 eV, corresponding to V^{5+} and V^{4+}, respectively [48]. Compared to VOH with 13% V^{4+} (Fig. S3b), higher-content V^{4+} (20%) is found in KVOH (Fig. S3a) achieving electronic neutrality after positive K^+ insertion. The atomic ratio of K to V is 1:12 by inductively coupled plasma (ICP) measurements. Based on ICP and XANES results, the molecular formula can be roughly estimated as $KV^{(V)}_{8.76}V^{(IV)}_{3.24}O_{28.88}{\cdot}nH_2O$ by imposing the requirement of electroneutrality upon K^+ insertion, with more low-valence V^{4+} and increased oxygen vacancies in the structure after K^+ incorporation. This phenomenon can be also observed in the previously published hydrated Mn^{2+} inserted vanadate [28].

Fig. 2a shows the galvanostatic charge/discharge (GCD) profiles of samples. At 0.05 A g^{-1}, KVOH demonstrates a discharge capacity of 436 mAh g^{-1}, which is higher than VOH of 369 mAh g^{-1}. KVOH also possesses a smaller voltage gap between charge and discharge profiles than VOH, indicating highly reactive reversibility and reduced polarization [49]. At a high current density of 5 A g^{-1}, KVOH still maintains its superiority in voltage gap and capacity. More GCD profiles at various current densities are shown in Fig. S4. Fig. 2b reports the corresponding rate performance of samples at various current densities. KVOH exhibits capacities of 408, 382, 351, 293 and 227 mAh g^{-1} at 0.5, 1, 2, 5 and 10 A g^{-1}, respectively. VOH shows lower values of 267, 253, 228, 187 and 149 mAh g^{-1} at 0.5, 1, 2, 5 and 10 A g^{-1}, respectively. The capacity gap exists between KVOH and VOH, up to 140 mAh g^{-1} at 0.5 A g^{-1} and 80 mAh g^{-1} at 10 A g^{-1}. The capacity enhancement of KVOH is attributed to higher electrochemical activity and more effective Zn^{2+} intercalation kinetics after K^+ introduction. Although some active sites could be occupied by K^+, the introduction of K^+ shows more significant effects on structure stability, which leads to more excellent electrochemical properties and device performance. As the current density is lowered back to 0.5 A g^{-1}, KVOH illustrates highly reversible capacities and retains the capacity gap with VOH. The capacity of KVOH is also superior to the published hydrated vanadates and vanadium oxides, e.g. $V_5O_{12}{\cdot}6H_2O$ [50] (355 mAh g^{-1} at 0.5 A g^{-1}), $K_2V_6O_{16}{\cdot}2.7H_2O$ [35] (237 mAh g^{-1} at 0.5 A g^{-1}, 178 mAh g^{-1} at 6 A g^{-1}), $K_2V_8O_{21}$ [34] (247 mAh g^{-1} at 0.3 A g^{-1}, 92 mAh g^{-1} at 4 A g^{-1}) and $Ca_{0.24}V_2O_5{\cdot}0.83H_2O$ [51] (340 mAh g^{-1} at 0.2 C). More detailed comparison of capacities is summarized in Table S1. The energy efficiency (EE) of samples was calculated based on the ratio of discharge to charge energy density shown in Fig. 2c, which is a crucial factor to evaluate the utility of batteries [52]. Generally, undesirable redox reactions and resistances and polarizations in batteries result in some irreversible discharge energy density, leading to the EE lower than 100%. In the inset of Fig. 2c, KVOH at 0.05 A g^{-1} exhibits a narrower voltage hysteresis between charge and discharge profiles, with a higher EE of 88% than VOH of 82%. And KVOH performs a higher EE with better reversibility than VOH even as the current density increases to 10 A g^{-1}. The Ragone plot in Fig. 2d reveals the relationship between energy density and the corresponding power density. KVOH possesses a comparable energy density of 308 Wh kg^{-1} at 402 W kg^{-1}, almost 1.5 times as VOH (201 Wh kg^{-1} at 375 W kg^{-1}), and significantly greater than $V_5O_{12}{\cdot}6H_2O$ [50] (194 Wh kg^{-1} at 2100 W kg^{-1}), $K_2V_6O_{16}{\cdot}2.7H_2O$ [35] (128 Wh kg^{-1} at 5760 W kg^{-1}) and $Ca_{0.24}V_2O_5{\cdot}0.83H_2O$ [51] (267 Wh kg^{-1} at 53.4 W kg^{-1}) and others shown in Table S1. Moreover, KVOH demonstrates a high power density of 7502 W kg^{-1} at 170 Wh kg^{-1} with infinite potential for high-rate and large-scale ZIBs. The cycling performance and corresponding Coulombic efficiency were performed at 5 A g^{-1} in Fig. 2e. KVOH delivers a high capacity of about 300 mAh g^{-1} at 5 A g^{-1} and keeps good stability with only 8% capacity decay after 3000 cycles whereas VOH with 28% capacity fading after just 1000 cycles. The capacity decay per cycle decreases to 0.0027% for KVOH, just one tenth of 0.028% of VOH. This is hypothesized that KVOH benefits from the introduction of K–O bond with more ionic character and higher binding energy than V–O bond, thus allowing enhanced interaction between layers and higher stability of the crystal structure. The fast capacity fading for VOH could be attributed to structure aggregation during long terms, which is difficult for adequate Zn^{2+} intercalation/deintercalation. Coulombic efficiency in the first cycle of KVOH is 80%, little lower than VOH of 85%. It can be explained that KVOH exhibits more side reactions

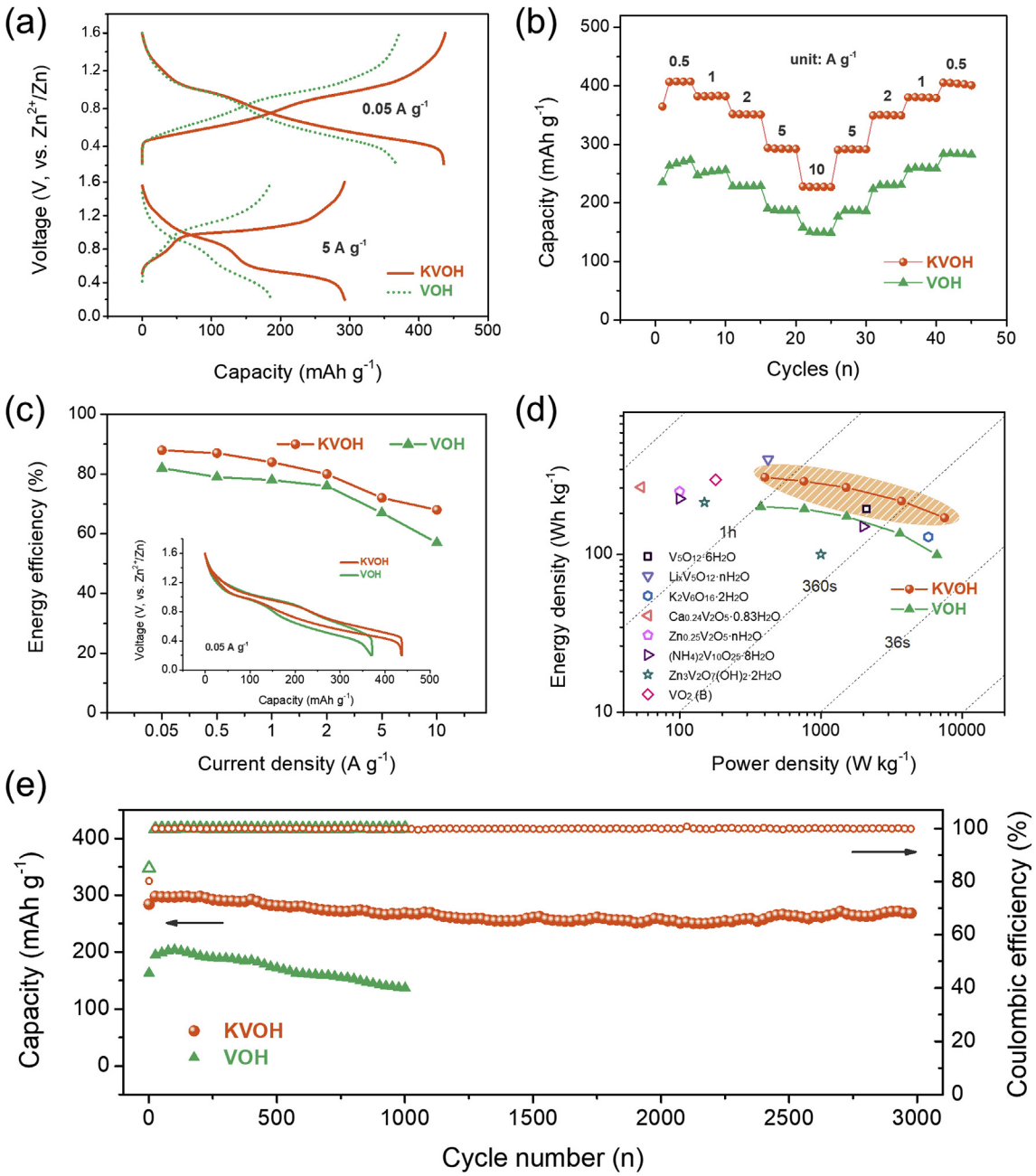

Fig. 2. (a) GCD profiles collected at 0.05 A g^{-1} and 5 A g^{-1} and (b) rate performance of both samples, the capacities were calculated based on the active mass of the cathode. (c) The energy efficiency of the batteries, inset of (c) is voltage hysteresis profiles of the cathode at 0.05 A g^{-1} in their corresponding batteries. (d) Ragone plot of the cathodes. (e) Cycling performance of samples tested at 5 A g^{-1}, KVOH shows great stability with 92% capacity retention even after 3000 cycles.

than VOH in Fig. 3a, which leads to lower Coulombic efficiency. After first cycle, KVOH and VOH show high Coulombic efficiency near to 100%. The SEM image of cycled KVOH cathode in Fig. S5a exhibits less aggregation than cycled VOH (Fig. S5b). Chemically K^+ incorporation can effectively modify the crystalline behavior and stabilize the material structure to achieve high reversibility and excellent cycling performance during the charge/discharge process, with excellent pragmatic value for next-generation portable electronics and electronic vehicles.

Fig. 3a shows the 1st cycle of CV curves at 0.1 mV s^{-1} of samples, both with two main pairs of redox peaks corresponding to multi-step Zn^{2+} insertion/extraction inducing redox reactions of V^{3+}/V^{4+} (β-β′) and V^{4+}/V^{5+}(α-α'). Other weak peaks result from some slight side reactions and disappear in the 2nd and 3rd cycles (Fig. S6), indicating excellent retention of the CV shape after the 1st cycle. KVOH possesses a higher open-circuit voltage of 1.30 V than VOH of 1.09 V. Comparing the 3rd cycle in Fig. 3b, the superiority of KVOH is evidenced by the larger response current related to the higher capacity, and more narrow overpotential gaps (V^{3+}/V^{4+}: 0.07 V, V^{4+}/V^{5+}: 0 V) with more reversible insertion/extraction kinetics. In KVOH, the centroid of the two redox peaks shifts to lower voltages, with 0.98 V for V^{4+}/V^{5+} and 0.525 V for V^{3+}/V^{4+}, compared to 1.005 V and 0.535 V for VOH, respectively. It could indicate the Gibbs free energy of the redox reactions changes after K^+ introduction. CV curves of KVOH at various scan rates were tested and are shown in Figs. S7 and b values were calculated, shown in Fig. 3c to estimate Zn^{2+} insertion/extraction belongs to either a diffusion-controlled or a surface-controlled process. The corresponding results for VOH are reported in Fig. S8. Theoretically, the relationship between the response current and the scan rate can be described by the following equation [53]:

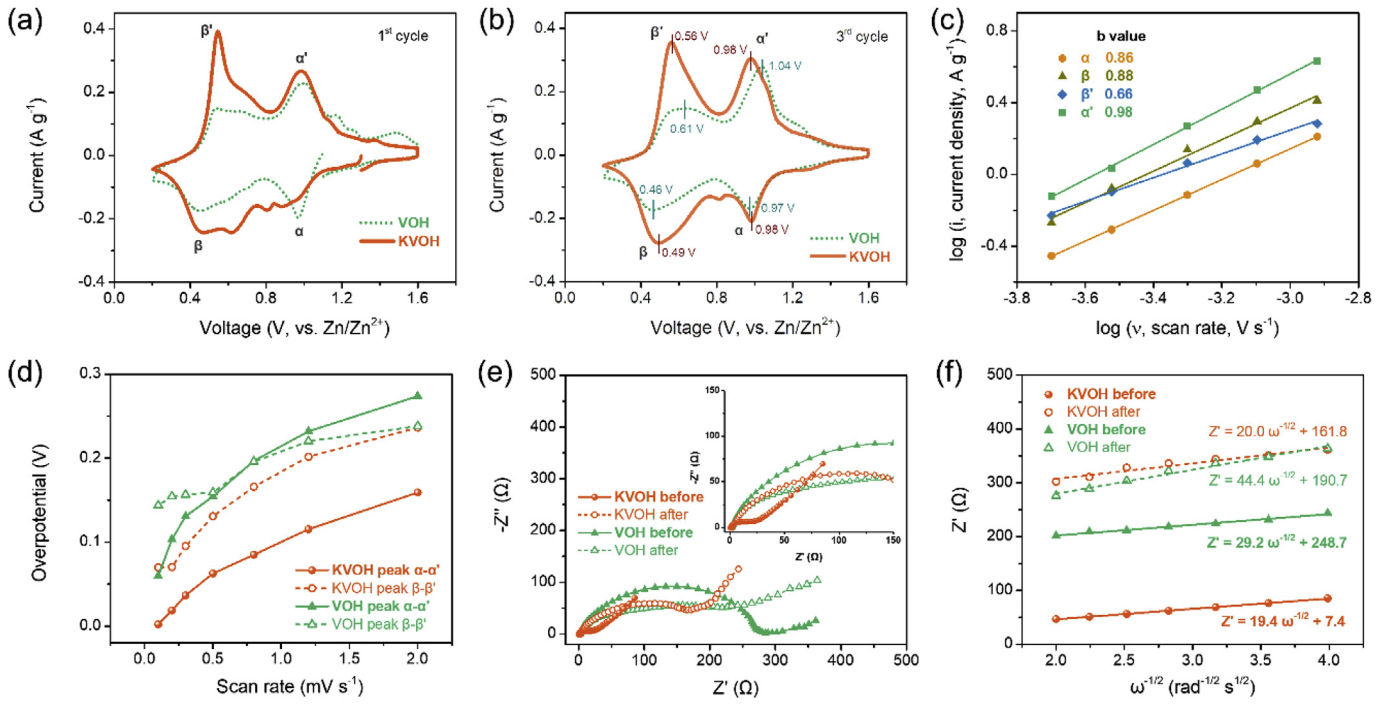

Fig. 3. CV curves at (a) 1st cycle and (b) 3rd cycle at 0.1 mV s^{-1} of samples. (c) b values of redox peaks, calculated by CV curves at various scan rates of KVOH. A larger slope indexes to a higher b value indicating a more surface-controlled process. (d) Overpotential gaps of redox pairs based on CV curves at various scan rates. (e) Nyquist plots of samples before and after cycling. (f) The relationship between the real part of impedance and low frequencies. The smaller slope means faster ion diffusion.

$$i = a\nu^b \quad (2)$$

where a and b are adjustable parameters. b = 1 corresponds to a surface-controlled process, while b = 0.5 is indicative of a diffusion-controlled process [54]. b values of different redox peaks of KVOH are between 0.5 and 1 indicating a hybrid diffusion-surface controlled process. Higher b values of KVOH than VOH reveal a higher contribution of a surface-controlled process for KVOH during charge/discharge cycles. KVOH also shows higher capacitive contributions than VOH at all scan rates in Fig. S9. It is beneficial to achieve faster ion diffusion, especially at high current densities or high scan rates. Fig. 3d performs the overpotential gaps of redox pairs at various scan rates. As scan rates increase, overpotential gaps broaden with more serious voltage hysteresis because of the limited reaction kinetics. KVOH maintains smaller gaps than VOH at all scan rates with smaller polarization and thus higher energy efficiency (confirmed in Fig. 2c). Fig. 3e and Fig. S10 show the EIS spectra of samples, with a semicircle at high frequencies and a linear part at low frequencies. Comparing the semicircular region, pristine KVOH before cycling shows a small diameter with a charge transfer resistance (R_{ct}) of 25.7 Ω, extremely lower than pristine VOH with 284.7 Ω. After 3 cycles, electrodes were activated, leading to reduced R_{ct} of both KVOH and VOH as shown in Fig. S10. After 3000 cycles, the R_{ct} of KVOH increases to 171.5 Ω, but is still smaller than VOH with 219.0 Ω (Fig. 3e). The linear part at low frequencies can be used to evaluate ion diffusion coefficients ($D_{Zn^{2+}}$) based on slope values in Fig. 3f (details in Experimental Section in SI) [55]. KVOH in the pristine state exhibits a higher $D_{Zn^{2+}}$ of 6.6×10^{-14} $cm^2\ s^{-1}$ than VOH of 2.9×10^{-14} $cm^2\ s^{-1}$ and retains the advantage after 3 cycles and after 3000 cycles, with 6.2×10^{-14} $cm^2\ s^{-1}$ higher than VOH of 1.3×10^{-14} $cm^2\ s^{-1}$. This can be explained that K^+ incorporation can efficiently introduce oxygen vacancies and motivate electron hoping between V^{4+} and V^{5+} to improve the conductivity of the electrode material and enhance its ion diffusion kinetics, and interact with oxygen in bilayer structure and interlayer water, playing a stabilizing role for long-term cycling.

The electrochemical properties of KVOH at different charge/discharge states are further studied. In Fig. 4a, pristine KVOH performs an urchin-like structure with an open-circuit voltage of 1.31 V. At the current density of 0.05 A g^{-1}, it is first discharged to 0.2 V achieving a fully discharged state and then charged to 1.6 V to reach a fully charged state. KVOH exhibits the dispersed nanosheets structure when fully discharged and reverses to microspheres with nanorods when fully charged, shown in SEM images inset of Fig. 4a. In Fig. 4b, the high-efficiency Zn^{2+} intercalation behavior at the fully discharged state from the pristine state can be observed, which is further confirmed by ICP results with Zn concentration of 20.57 mg L^{-1} and a V: Zn atomic ratio of 1: 0.87. The intensity of Zn 2p peak reduces after Zn^{2+} deintercalation at fully charged state with Zn concentration of 7.75 mg L^{-1} and the atomic ratio of V to Zn is 1: 0.25. It should be mentioned that the Zn concentration measured by ICP could be higher than the real content of Zn^{2+} inserted in the structure due to the difficulty of removing surface-adsorbed Zn^{2+} from materials. The detected intensity is caused by inevitable adsorbed Zn^{2+} on the electrode surface. V K-edge XANES spectra of KVOH at different charge/discharge states are recorded in Fig. 4c, the shaded area is magnified in Fig. 4d. In the fully discharged state, V^{5+} is reduced to lower-valence V^{4+} and V^{3+} after Zn^{2+} insertion to maintain electronic neutrality. This reflects in the XANES results by a shift of the energy edge position approaching to the V^{4+} K-edge position. The pre-edge peaks are also observed to shift and their corresponding intensities decay which is consistent with the V^{4+} and V^{3+} ions occupying fewer 3 d orbitals than V^{5+} [47,56]. The lattice spacing is extended accordingly, which is reflected by the XRD patterns in Fig. 4e displaying peaks shift to smaller angles. TEM images with elemental mappings in Fig. 4f reveal a homogeneous Zn distribution in structure. At the fully charged state, V^{4+} and V^{3+} are oxidized to higher-valence V^{5+} after Zn^{2+} extraction, with the edge shifting to higher energies similar to the pristine state. XRD pattern of KVOH at the full charged state confirms it further, with diffraction peaks shifting to larger angles. Therefore, KVOH is stretchable for adequate Zn^{2+} insertion and reversibly contract to recover the pristine structure albeit with a reduced lattice spacing compared to VOH. The excellent accommodation of KVOH to structural transformation during ion insertion/extraction reveals vast potential for high-performance and

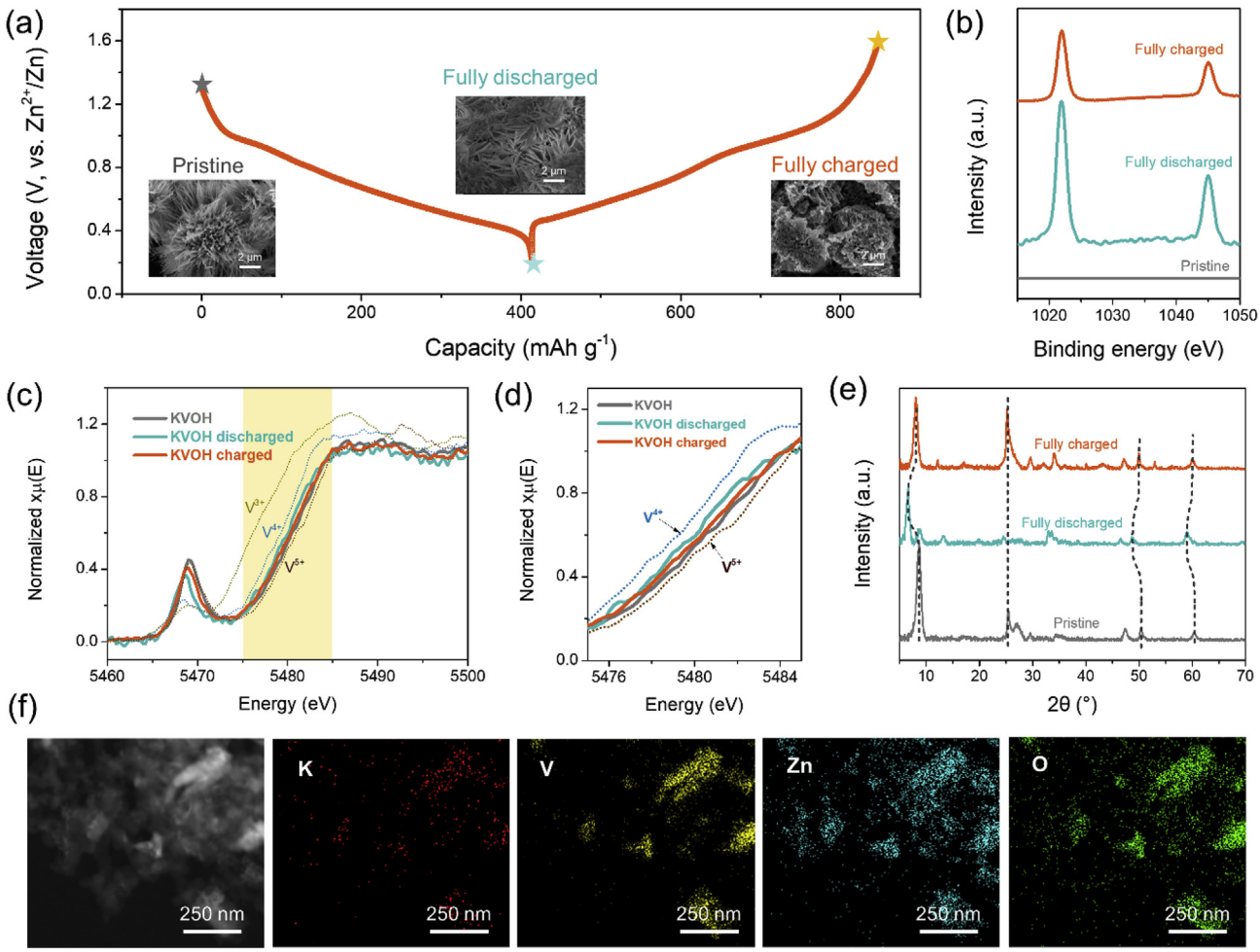

Fig. 4. (a) GCD profiles at the 1st cycle at 0.05 A g^{-1}. The inset of (a) is SEM images of KVOH at different charge/discharge states. (b) Zn 2p XPS spectra and (c) V K-edge XANES spectra of KVOH at different charge/discharge states. (d) The magnified pattern of the shaded area in (c). (e) XRD patterns of KVOH at different charge/discharge states. (f) TEM elemental mappings of KVOH at fully discharged, elemental Zn can be clearly detected in KVOH structure.

long-life secondary batteries.

3. Conclusions

K^+ incorporated hydrated vanadate ($KV_{12}O_{30-y}{\cdot}nH_2O$, KVOH) is fabricated to achieve an electrochemically stable structure for long-term efficient ion diffusion as a result of structural engineering. K^+ introduction leads to a contracted interlayer spacing of 9.9 Å compared to hydrated vanadium pentoxide ($V_2O_5{\cdot}nH_2O$, VOH) of 12.0 Å. The contracted structure is stretchable to 13.2 Å when Zn^{2+} inserted and recovers to 10.9 Å when Zn^{2+} extracted, with fast Zn^{2+} diffusion kinetics even at high rates. K^+ also plays a crucial role in increasing mechanical strength and preventing structural collapse during long-term charge/discharge cycles. KVOH as a ZIB cathode exhibits an enhanced capacity of 436 mAh g^{-1} at 0.05 A g^{-1}, which is higher than VOH of 369 mAh g^{-1}. KVOH maintains great stability with only 8% capacity decay after 3000 cycles at 5 A g^{-1} while VOH suffers a 20% fading after 1000 cycles. KVOH also exhibits both high energy density (308 Wh kg^{-1} at 402 W kg^{-1}) and high power density (7502 W kg^{-1} at 170 Wh kg^{-1}). Consequently, KVOH possesses tremendous value as a cathode material for next-generation energy storage systems.

Declaration of competing interest

The authors declare that they have no known competing financial interests or personal relationships that could have appeared to influence the work reported in this paper.

CRediT authorship contribution statement

Meng Tian: Conceptualization, Methodology, Writing - original draft. **Chaofeng Liu:** Conceptualization, Methodology, Writing - review & editing. **Jiqi Zheng:** Visualization, Resources. **Xiaoxiao Jia:** Validation. **Evan P. Jahrman:** Formal analysis, Writing - review & editing. **Gerald T. Seidler:** Writing - review & editing. **Donghui Long:** Supervision. **Muhammad Atif:** Funding acquisition. **Mohamad Alsalhi:** Funding acquisition. **Guozhong Cao:** Supervision, Writing - review & editing, Funding acquisition.

Acknowledgments

This work was supported by the National Science Foundation (CBET-1803256), National Science Foundation of China (No. 21576090), and Fundamental Research Funds for the Central Universities (222201718002). Part of this work was conducted at the Molecular Analysis Facility, a National Nanotechnology Coordinated Infrastructure site at the University of Washington which is supported in part by the National Science Foundation (grant NNCI-1542101), the University of Washington, the Molecular Engineering & Sciences Institute, and the Clean Energy Institute. MT and JZ acknowledge the financial support from CSC for this work at the University of Washington. EPJ was supported by a subcontract from the National Institute of Standards and

Technology (NIST). Opinions, recommendations, findings, and conclusions presented in this manuscript and associated materials do not necessarily reflect the views or policies of NIST or the United States Government. The authors also extend their appreciation to the International Scientific Partnership Program (ISPP) at King Saud University for funding this research work through ISPP-139.

Appendix A. Supplementary data

Supplementary data to this article can be found online at https://doi.org/10.1016/j.ensm.2020.03.024.

References

[1] M. Armand, J. Tarascon, Building better batteries, Nature 451 (2008) 2–7.
[2] B. Dunn, H. Kamath, J. Tarascon, Electrical energy storage for thegrid : a battery of choices, Science 334 (2011) 928–936.
[3] C. Liu, J. Yuan, R. Masse, X. Jia, W. Bi, Z. Neale, Interphases, Interfaces, and Surfaces of Active Materials in Rechargeable Batteries and Perovskite Solar Cells, 2020, pp. 1–29, 1905245.
[4] J.B. Goodenough, Y. Kim, Challenges for rechargeable Li batteries, Chem. Mater. 22 (2010) 587–603.
[5] Y. Liang, W.-H. Lai, Z. Miao, S.-L. Chou, Nanocomposite materials for the sodium–ion battery: a review, Small (2018) 1–20, 1702514.
[6] G. Fang, J. Zhou, A. Pan, S. Liang, Recent advances in aqueous zinc–ion batteries, ACS Energy Lett 3 (2018) 2480–2501.
[7] V. Verma, S. Kumar, W.M. Jr, R. Satish, M. Srinivasan, Progress in rechargeable aqueous zinc– and aluminum–ion battery electrodes : challenges and outlook, Adv. Sustain. Syst. (2019) 1–33, 1800111.
[8] Y. Li, J. Fu, C. Zhong, T. Wu, Z. Chen, W. Hu, K. Amine, J. Lu, Recent advances in flexible zinc–based rechargeable batteries, Adv. Energy Mater. (2019) 1–9, 1802605.
[9] X. Guo, G. Fang, W. Zhang, J. Zhou, L. Shan, L. Wang, C. Wang, T. Lin, Y. Tang, S. Liang, Mechanistic insights of Zn^{2+} storage in sodium vanadates, Adv. Energy Mater. (2018) 1–7, 1801819.
[10] D. Chao, W. Zhou, C. Ye, Q. Zhang, Y. Chen, Gu Lin, K. Davey, S.-Z. Qiao, An electrolytic Zn–MnO_2 battery demonstrated for high-voltage and scalable energy storage, Angew. Chem. Int. Ed. (2019) 7823.
[11] Q. Pang, C. Sun, Y. Yu, K. Zhao, Z. Zhang, P.M. Voyles, G. Chen, Y. Wei, X. Wang, $H_2V_3O_8$ nanowire/graphene electrodes for aqueous rechargeable zinc ion batteries with high rate capability and large capacity, Adv. Energy Mater. (2018) 1–9, 1800144.
[12] H. Qin, L. Chen, L. Wang, X. Chen, Z. Yang, V_2O_5 hollow spheres as high rate and long life cathode for aqueous rechargeable zinc ion batteries, Electrochim. Acta 306 (2019) 307–316.
[13] J. Zheng, C. Liu, M. Tian, X. Jia, E.P. Jahrman, G.T. Seidler, S. Zhang, Y. Liu, Y. Zhang, C. Meng, G. Cao, Fast and reversible zinc ion intercalation in Al–ion modified hydrated vanadate, Nano Energy 70 (2020) 104519.
[14] T. Xiong, Z.G. Yu, H. Wu, Y. Du, Q. Xie, J. Chen, Y. Zhang, S.J. Pennycook, W. Siang, V. Lee, J. Xue, Defect engineering of oxygen–deficient manganese oxide to achieve high-performing aqueous zinc ion battery, Adv. Energy Mater. (2019) 1–9, 1803815.
[15] H. Pan, Y. Shao, P. Yan, Y. Cheng, K.S. Han, Z. Nie, C. Wang, J. Yang, X. Li, P. Bhattacharya, K.T. Mueller, J. Liu, Reversible aqueous zinc/manganese oxide energy storage from conversion reactions, Nat. Energy. 1 (2016) 16039.
[16] L. Zhang, L. Chen, X. Zhou, Z. Liu, Towards high-voltage aqueous metal-ion batteries beyond 1.5 V : the zinc/zinc hexacyanoferrate system, Adv. Energy Mater. 5 (2015) 1400930–1400934.
[17] R. Trócoli, F. La, An Aqueous Zinc-ion battery based on copper hexacyanoferrate, ChemSusChem 8 (2015) 481–485.
[18] S. Islam, H. Alfaruqi, V. Mathew, J. Song, Facile synthesis and the exploration of the zinc storage mechanism of β–MnO_2 nanorods with exposed (101) planes as a novel cathode material for high performance eco-friendly zinc–ion batteries, J. Mater. Chem. A. 5 (2017) 23299–23309.
[19] L. Zhang, L. Chen, X. Zhou, Z. Liu, Morphology-dependent electrochemical performance of zinc hexacyanoferrate cathode for zinc-ion battery, Sci. Rep. 5 (2015) 18263.
[20] H. Wang, X. Bi, Y. Bai, C. Wu, S. Gu, S. Chen, F. Wu, K. Amine, J. Lu, Open–structured $V_2O_5{\cdot}nH_2O$ nanoflakes as highly reversible cathode material for monovalent and multivalent intercalation batteries, Adv. Energy Mater. (2017) 1–8, 1602720.
[21] J. Ding, Z. Du, L. Gu, B. Li, L. Wang, S. Wang, Y. Gong, Ultrafast Zn^{2+} intercalation and deintercalation in vanadium dioxide, Adv. Mater. (2018) 2–7, 1800762.
[22] T. Wei, Q. Li, G. Yang, C. Wang, An electrochemically induced bilayered structure facilitates long–life zinc storage of vanadium dioxide, J. Mater. Chem. A. 6 (2018) 8006–8012.
[23] D. Chao, C. Zhu, Rose, M. Song, P. Liang, X. Zhang, N. Tiep, Huy, H. Zhang, H.J. Fan, High-rate and stable quasi–solid–state zinc-ion battery with novel 2D layered zinc orthovanadate array, Adv. Mater. 32 (2018) 1803181.
[24] L. Shan, Y. Yang, W. Zhang, H. Chen, G. Fang, J. Zhou, S. Liang, Observation of combination displacement/intercalation reaction in aqueous zinc–ion battery, Energy Storage Mater 18 (2019) 10–14.
[25] X. Liu, H. Zhang, D. Geiger, J. Han, A. Varzi, U. Kaiser, A. Moretti, S. Passerini, Calcium vanadate sub–microfibers as highly reversible host cathode material for aqueous zinc–ion batteries, Chem.Commun. 55 (2019) 2265–2268.
[26] M. Yan, P. He, Y. Chen, S. Wang, Q. Wei, K. Zhao, Water-lubricated intercalation in $V_2O_5{\cdot}nH_2O$ for high–capacity and high–rate aqueous rechargeable zinc batteries, Adv. Mater. 1703725 (2018) 1–6.
[27] Q. An, Y. Li, H. Deog, S. Chen, Q. Ru, L. Mai, Y. Yao, Graphene decorated vanadium oxide nanowire aerogel for long–cycle–life magnesium battery cathodes, Nano Energy 18 (2015) 265–272.
[28] C. Liu, Z. Neale, J. Zheng, X. Jia, J. Huang, M. Yan, M. Tian, M. Wang, J. Yang, G. Cao, Expanded hydrated vanadate for high–performance aqueous zinc–ion batteries, Energy Environ. Sci. 12 (2019) 2273–2285.
[29] M. Song, H. Tan, D. Chao, H.J. Fan, Recent Advances in Zn–Ion Batteries, 2018, pp. 1–27, 1802564.
[30] A.J. He, X. Liu, H. Zhang, Z. Yang, X. Shi, Q. Liu, X. Lu, Enhancing Zn-ion storage capability of hydrated vanadium pentoxide by the strategic introduction of La^{3+}, ChemSusChem 13 (6) (2019) 1568–1574.
[31] J. Meng, Z. Liu, C. Niu, X. Xu, X. Liu, G. Zhang, X. Wang, M. Huang, Y. Yu, L. Mai, A synergistic effect between layer surface configurations and K ions of potassium vanadate nanowires for enhanced energy storage, J. Mater. Chem. A. 4 (2016) 4893–4899.
[32] S. Islam, H. Alfaruqi, B. Sambandam, A new rechargeable battery based on a zinc anode and a NaV_6O_{15} nanorod cathode, Chem.Commun. 55 (2019) 3793–3796.
[33] Y. Zhao, C. Han, J. Yang, J. Su, X. Xu, S. Li, L. Xu, R. Fang, H. Jiang, X. Zou, B. Song, L. Mai, Q. Zhang, Stable alkali metal ion intercalation compounds as optimized metal oxide nanowire cathodes for lithium batteries, Nano Lett. 15 (2015) 2180–2185.
[34] B. Tang, G. Fang, J. Zhou, L. Wang, Y. Lei, C. Wang, Potassium vanadates with stable structure and fast ion diffusion channel as cathode for rechargeable aqueous zinc–ion batteries, Nano Energy 51 (2018) 579–587.
[35] B. Sambandam, V. Soundharrajan, S. Kim, M.H. Alfaruqi, J. Jo, S. Kim, V. Mathew, $K_2V_6O_{16}{\cdot}2.7H_2O$ nanorod cathode: an advanced intercalation system for high energy aqueous rechargeable Zn–ion batteries, J. Mater. Chem. A. 6 (2018) 15530–15539.
[36] B.C. Melot, J. Tarascon, Design and preparation of materials for advanced electrochemical storage, Acc. Chem. Res. 46 (2013) 1226–1238.
[37] C. Liu, C. Zhang, H. Fu, X. Nan, G. Cao, Exploiting high-performance anode through tuning the character of chemical bonds for Li-ion batteries and capacitors, Adv. Energy Mater. 7 (2017) 1601127.
[38] W.D. Calister, Fundamentals of Materials Science and Engineering, John Wiley & Sons, Inc, 2001.
[39] C. Sanchez, J. Livage, G. Lucazeau, Infrared and Raman study of amorphous V_2O_5, J. Raman Spectrosc. 12 (1982) 3–7.
[40] S. Boukhalfa, K. Evanoff, G. Yushin, Atomic layer deposition of vanadium oxide on carbon nanotubes for high–power supercapacitor electrodes, Energy Environ. Sci. 5 (2012) 6872.
[41] J. Lee, S. Badie, P. Srimuk, A. Ridder, H. Shim, S. Choudhury, Y.-C. Nah, V. Presser, Electrodeposition of hydrated vanadium pentoxide on nanoporous carbon cloth for hybrid energy storage, Sustain. Energy Fuels. 2 (2018) 577.
[42] S. Lee, H.M. Cheong, M. Je, P. Liu, C.E. Tracy, A. Mascarenhas, J.R. Pitts, S.K. Deb, Raman spectroscopic studies of amorphous vanadium oxide thin films, Solid State Ionics 165 (2003) 111–116.
[43] G.T. Seidler, D.R. Mortensen, A.J. Remesnik, J.I. Pacold, N.A. Ball, N. Barry, M. Styczinski, O.R. Hoidn, A laboratory-based hard X–ray monochromator for high–resolution X–ray emission spectroscopy and X–ray absorption near edge structure measurements, Rev. Sci. Instrum. 85 (2014) 113906.
[44] E.P. Jahrman, W.M. Holden, A.S. Ditter, D.R. Mortensen, G.T. Seidler, T.T. Fister, S.A. Kozimor, L.F.J. Piper, J. Rana, N.C. Hyatt, M.C. Stennett, An improved laboratory–based X–ray absorption fine structure and X–ray emission spectrometer for analytical applications in materials chemistry, Rev. Sci. Instrum. 113906 (2019), 024106.
[45] R. Bacewicz, M. Wasiucionek, A. Twarog, P. Filipowicz, P. Jozwiak, J. Garbarczyk, A XANES study of the valence state of vanadium in lithium vanadate phosphate glasses, J. Mater. Sci. 40 (2005) 4267–4270.
[46] A. Gaur, B.D. Shrivastava, Speciation using X ray absorption fine structure (XAFS), Rev. J. Chem. 5 (2015) 361–398.
[47] W. Avansi, L.J.Q. Maia, C. Ribeiro, E.R. Leite, V.R. Mastelaro, Local structure study of vanadium pentoxide, J Nanopart Res 13 (2011) 4937–4946.
[48] F. Liu, Z. Chen, G. Fang, Z. Wang, Y. Cai, B. Tang, V_2O_5 nanospheres with mixed vanadium valences as high electrochemically active aqueous zinc–ion battery cathode, Nano-Micro Lett. 11 (2019) 25.
[49] G. Fang, C. Zhu, M. Chen, J. Zhou, B. Tang, X. Cao, Suppressing manganese dissolution in potassium manganate with rich oxygen defects engaged high-energy-density and durable aqueous zinc–ion battery, Adv. Funct. Mater. (2019) 1–9, 1808375.
[50] N. Zhang, M. Jia, Y. Dong, Y. Wang, J. Xu, Y. Liu, Hydrated layered vanadium oxide as a highly reversible cathode for rechargeable aqueous zinc batteries, Adv. Funct. Mater. (2019) 1–9, 1807331.
[51] Z. Batteries, C. Xia, J. Guo, P. Li, X. Zhang, H.N. Alshareef, Highly stable aqueous zinc-ion storage using a layered calcium vanadium oxide bronze cathode, Angew. Chem. Int. Ed. 57 (2018) 3943–3948.
[52] C. Liu, S. Wang, C. Zhang, H. Fu, X. Nan, Y. Yang, High power high safety battery with electrospun $Li_3V_2(PO_4)_3$ cathode and $Li_4Ti_5O_{12}$ anode with 95% energy efficiency, Energy Storage Mater 5 (2016) 93–102.

[53] T. Yuan, Y. Jiang, W. Sun, B. Xiang, Y. Li, M. Yan, B. Xu, Ever–increasing pseudocapacitance in rGO–MnO–rGO sandwich nanostructures for ultrahigh–rate lithium storage, Adv. Funct. Mater. 26 (2016) 2198–2206.
[54] C. Yang, Y. Zhang, J. Zhou, C. Lin, F. Lv, K. Wang, J. Feng, Z. Xu, J. Li, S. Guo, Hollow Si/SiOx nanosphere/nitrogen–doped carbon superstructure with a double shell and void for high–rate and long–life lithium–ion storage, J. Mater. Chem. A. 6 (2018) 8039–8046.
[55] P. Hu, T. Zhu, X. Wang, X. Wei, M. Yan, J. Li, W. Luo, W. Yang, W. Zhang, L. Zhou, Z. Zhou, L. Mai, Highly durable $Na_2V_6O_{16}{\cdot}1.63H_2O$ nanowire cathode for aqueous zinc–ion battery, Nano Lett. 18 (2018) 1758–1763.
[56] G. Bunker, Introduction to XAFS, Cambridge Univ. Press, 2010.